Available online at www.sciencedirect.com
SCIENCE DIRECT®
PERGAMON
International Journal of Heat and Mass Transfer 46 (2003) 4257–4269
International Journal of HEAT and MASS TRANSFER
www.elsevier.com/locate/ijhmt

Semi-analytical model for boiling from enhanced structures

C. Ramaswamy [a], Y. Joshi [b,*], W. Nakayama [c], W.B. Johnson [d]

[a] IBM Corporation, Hopewell Junction, NY 12533, USA
[b] G.W. Woodruff School of Mechanical Engineering, Georgia Institute of Technology, Atlanta, GA 30332, USA
[c] ThermTech International, Kanagawa 255-0004, Japan
[d] Laboratory for Physical Sciences, College Park 20740, USA

Received 14 January 2002; received in revised form 11 April 2003

Abstract

Understanding of the fundamental mechanism of boiling from enhanced structures is currently incomplete. The main focus of the present study was to develop a semi-analytical model to predict the bubble departure diameter, frequency, and nucleation site density for a boiling enhancement structure. Existing models in literature were used as a framework to develop this. Salient feature of the model is the improvements on sub-models for bubble departure diameter, evaporation within the channels and convective heat transfer from the external surfaces of the enhanced structure. The model was used to calculate the total heat dissipated from the structures. Comparisons to experiments revealed that the bubble departure is predicted within ±10%, frequency within ±30% for all data points except a couple, nucleation site density within ±40% and the heat flux within ±50%. Sample calculations have been included to show its use in optimizing the geometrical parameters for maximizing heat transfer.

1. Introduction

The enhancement in heat transfer using structured surfaces has been demonstrated sufficiently in literature [1,2]. However, there are only few studies on modeling boiling from such structures. Nakayama et al. [3] were the first to develop a semi-empirical model. They carried out visualization studies on a structure that had rectangular channels (0.15–0.25 mm) covered with a thin plate (~100 μm) with pores (0.03–0.2 mm diameter) at a constant pitch (0.6–0.72 mm). They hypothesized that the main mechanism of boiling inside the channels was 'suction–evaporation', wherein a thin meniscus of liquid evaporated at the sharp corners and generated the bubbles at the pores. Using the experimental data, a semi-empirical model was developed, which included equations for the bubble departure diameter, frequency, and total heat flux from the structure. The semi-analytical model of Nakayama et al. [3] had six empirical constants. Chien and Webb [4] used a similar framework and modified several features of the existing model to reduce the empirical constants. Salient improvements in the model included tracking the liquid menisci radius inside the channels as a function of time, calculating the bubble departure diameter based on a force balance and calculating the heat flux from the external surfaces using an improved model developed by Haider and Webb [5]. Both of these studies [3,4] validated the models for a narrow range of wall superheats (0–4 °C). The current study builds on the previous models to predict the bubble dynamics from a single layered enhanced structure for a wider range of wall superheats. The enhanced structure consists of an array of rectangular channels on opposite sides of a silicon substrate. The channel depth is more than half the substrate thickness and by aligning the channels on either side orthogonal to each other, pores are created at the intersection points (Fig. 1).

In the studies by Nakayama et al. [3] and Chien and Webb [4], the bubbles emerge from the pores in an unbounded liquid. In the current study, the channel walls bound a growing bubble on two sides initially. However, high-speed visualization showed that the bubbles eventually emerge on the external surface and

* Corresponding author. Tel.: +1-40-4-385-2810; fax: +1-40-4-894-8496.
E-mail address: yogendra.joshi@me.gatech.edu (Y. Joshi).

0017-9310/$ - see front matter © 2003 Elsevier Ltd. All rights reserved.
doi:10.1016/S0017-9310(03)00216-3

Nomenclature

A	area (m^2)
A_{cyc}	volume of liquid evaporated/length for one bubble cycle (m^2)
A_m	meniscus area (m^2)
A'	proportionality constant for inertia driven bubble growth (Eq. (2))
c	empirical constant for modeling external convection (Eq. (41))
c_p	specific heat of liquid (J/kg K)
C_H	Hamaker constant, Eq. (14)—(J)
C_L	empirical constant for the lift force (Eq. (8))
C_s	empirical constant for unsteady growth force (Eq. (1))
C_{tl}	empirical constant for the rate of evaporation inside tunnels (Eq. (29))
C_{tg}	empirical constant for the growth rate (Eq. (35))
D	instantaneous diameter (mm)
f	frequency (Hz)
F	force (N)
g	acceleration due to gravity (9.81 m/s^2)
h_{fg}	latent heat of vaporization (J/kg)
H	height (mm)
k	thermal conductivity (W/m K)
L	length of the tunnel (mm)
m	mass (kg)
n_s	nucleation site density (m^{-2})
N_b	number of bubbles generated
N_m	number of menisci
N_p	number of pores/channel
P	pressure (Pa)
P_p	pore pitch (mm)
Pr	Prandtl number
q''	heat flux (W/cm^2)
Q	heat dissipation (W)
r_m	instantaneous meniscus radius (μm)
$r_{m,i}$	initial meniscus radius (μm)
$r_{m,e}$	final meniscus radius (μm)
r_{ne}	non-evaporating meniscus radius (μm)
R	instantaneous bubble radius (mm)
$\mathbf{R}$	particular gas constant (J/kg K)
$\dot{R}$, v_g	velocity at center of bubble—dR/dt (m/s)
$\ddot{R}$	acceleration at center of bubble—d^2R/dt^2 (m/s^2)
s	average separation distance between bubbles (mm)
t	time (s)
t_c	thickness of cover plate (mm)
T	temperature (°C)
T_w	local wall temperature (°C)
T_s	local saturation temperature (°C)
v_d	bubble rise velocity (m/s)
v_n	velocity of bubble front (m/s)
v_t	terminal velocity of bubble in a liquid pool (m/s)
V	volume (m^3)
W_t	channel width (mm)

Greek symbols

δ	meniscus thickness (μm)
Δ	difference in two quantities
ϕ	angle from the vertical axis for meniscus thickness evaluation (degrees)
ρ	density (kg/m^3)
σ	surface tension (m/s)
θ	contact angle (deg)

Subscripts

b	bubble
bi	bubble inertia
B	buoyancy
d	departure
duy	unsteady growth
e	intake
ex	external surface
exp	experimental
g	growth
l	liquid
li	liquid inertia
L	lift
m	meniscus
ne	non-evaporating
p	pore
pred	predicted
sat	saturation
st	surface tension
sup	superheat
t	channel (or tunnel)
v	vapor
vm	mean vapor
w	waiting
wall	at the bottom of the enhanced structure

are spherical in shape. The visualization studies showed that the diameter of the bubble (where it attaches to the top surface of the structure) was approximately equal to the pore diameter. Hence, it is hypothesized in this study that the bubble growing on the external surface is attached to the pore by a cylindrical stem whose diameter is same as that of the pore and height equal to the channel depth.

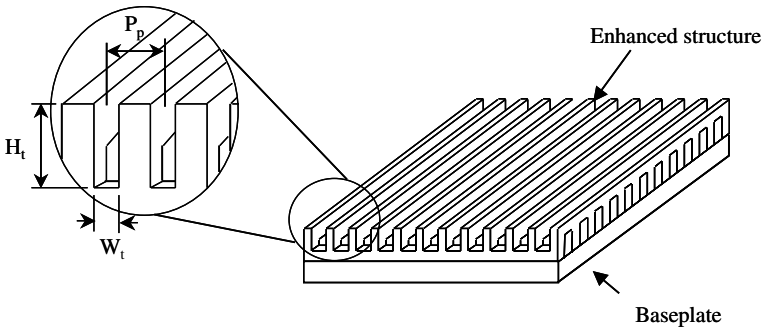

Fig. 1. Enhanced structures employed in this study.

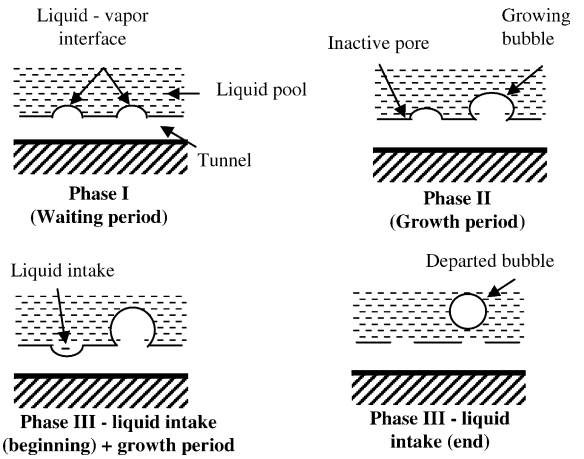

Fig. 2. Phases in a bubble growth and departure cycle.

The four essential parameters to quantify the boiling process are bubble departure diameter (D_d), frequency (f), nucleation site density (n_s) and the dissipated heat flux (q''). The frequency is defined as the inverse of the total time for one bubble cycle. Each bubble cycle consists of a waiting period (Δt_w), a growth period (Δt_g) and a liquid intake period (Δt_e) (see Fig. 2). There is some overlap between the growth period and the liquid intake period. Both Nakayama et al. [3] and Chien and Webb [4] found that the liquid intake period is very short compared to the other two and neglected it in their analytical models. The authors' visualization studies confirm this and hence the current model does not include the liquid intake period. The total heat flux is made up of two parts, evaporation inside the tunnels (q''_t) and enhanced convection on the external surfaces (q''_{ex}). Modeling of all these parameters is outlined in the following sections.

2. Semi-analytical model

2.1. Modeling bubble departure diameter

Most models for bubble departure from plain surfaces consider only the static forces during bubble growth. Klausner et al. [6] developed a comprehensive model for predicting the bubble departure diameters in flow boiling from plain surfaces. Zeng et al. [7] used these expressions to predict bubble departure diameters in pool boiling. Based on the magnitude of the various forces they concluded that for pool boiling, only the buoyancy and drag due to unsteady growth are important. One of their assumptions was that at departure the contact diameter approaches near zero due to necking at the cavity mouth. Based on this assumption they neglected the surface tension force. In a recent study, Sharma [8] pointed out that the liquid inertia force and the bubble inertia force are also important in addition to the forces mentioned above. All the above mentioned studies assume the growth rate to be heat transfer controlled and the instantaneous diameter was assumed to be proportional to the square root of time.

In enhanced structures, the bubbles are generated primarily because of evaporation of liquid menisci inside the tunnels and hence the process is inertia driven [9]. Based on the observations of Chien and Webb [9] and the present authors, the departing bubbles were found to be spherical in shape and attaching to the surface pore with a finite contact angle, unlike a flattened out bubble with a low contact angle for plain surfaces. Hence the necking phenomenon is not valid for the enhanced structures and the surface tension force cannot be neglected. The flow visualization studies also show that the departing bubble has a tendency to drag the next bubble growing at the same pore and hence the lift force due to wake of the departing bubble is also important. The expressions for the different forces (unsteady growth, buoyancy, surface tension, lift force, bubble inertia and liquid inertia) are given below.

(a) *Unsteady growth force (F_{duy}):* The expression for the growth force was developed by Zeng et al. [7] as

$$F_{\mathrm{duy}} = \rho_l \pi R^2 \left(\tfrac{3}{2} C_s \dot{R}^2 + R\ddot{R} \right) \tag{1}$$

where the constant C_s was found to be equal to 20/3. For an inertia driven growth

$$R = A't \tag{2}$$

where A' is a function of the wall superheat, geometry and properties of the fluid.

Combining Eqs. (1) and (2), the expression for growth force can be written as

$$F_{\mathrm{duy}} = \tfrac{3}{2}\rho_{\mathrm{l}}\pi A'^{2} C_{\mathrm{s}} R^{2} \tag{3}$$

(b) *Buoyancy force (F_B):* The buoyancy force on a bubble is given as

$$F_{\mathrm{B}} = (\rho_{\mathrm{l}} - \rho_{\mathrm{v}}) g V_{\mathrm{b}} \tag{4}$$

where V_{b} is the truncated bubble volume at departure (Fig. 3) and is given as

$$V_{\mathrm{b}} = \frac{\pi}{3}\left(\frac{D^3}{4} + \frac{D^2}{4}\sqrt{D^2 - D_{\mathrm{p}}^2} + \frac{D_{\mathrm{p}}^2}{8}\sqrt{D^2 - D_{\mathrm{p}}^2}\right) \tag{5}$$

(c) *Surface tension force (F_{st}):* The surface tension force is formulated similar to Chien and Webb [4]. Based on a simple geometrical analysis from Fig. 3, the contact angle θ is evaluated as

$$\theta = \sin^{-1}\left(\frac{D_{\mathrm{p}}}{D}\right) \tag{6}$$

The surface tension force is then given as

$$F_{\mathrm{st}} = \sigma\pi D_{\mathrm{p}} \sin(\theta) \tag{7}$$

(d) *Lift force (F_L):* The lift force on a bubble is modeled similar to Kolev [10]. The expression for this force can be written as

$$F_{\mathrm{L}} = \frac{\pi}{2}\rho_{\mathrm{l}}(D v_{\mathrm{d}})^2 C_{\mathrm{L}} \tag{8}$$

The rising bubbles induce a flow which has a rise velocity of v_{d}. The velocity was assumed to be approximately equal to $2\mathrm{d}R/\mathrm{d}t$ [7]. Hence the lift force can be rewritten as

$$F_{\mathrm{L}} = 2\pi\rho_{\mathrm{l}}(DA')^2 C_{\mathrm{L}} \tag{9}$$

The coefficient C_{L} was found by fitting the bubble departure diameters obtained from one set of visualization experiments [11] to the predictions based on the above forces. A value of 1.2 was found to predict the bubble departure diameters within 5% for that set of data. The predictions for other structures are presented in a later section in this paper.

(e) *Bubble inertia force (F_{bi}):* Sharma [8] used the following expression for the bubble inertia force:

$$F_{\mathrm{bi}} = m_{\mathrm{v}}\frac{\mathrm{d}v_{\mathrm{g}}}{\mathrm{d}t} + v_{\mathrm{g}}\frac{\mathrm{d}m}{\mathrm{d}R}\frac{\mathrm{d}R}{\mathrm{d}t} \tag{10}$$

For a linear bubble growth rate, the acceleration term $\mathrm{d}v_{\mathrm{g}}/\mathrm{d}t = 0$. The velocity at the bubble center, $v_{\mathrm{g}} = \mathrm{d}R/\mathrm{d}t$ [12]. The term $\mathrm{d}R/\mathrm{d}t$ can be obtained by differentiating Eq. (5) and multipying the resulting expression with the vapor density (ρ_{v}). Combining Eqs. (2), (5) and (10) gives

$$F_{\mathrm{bi}} = A'^{2}\rho_{\mathrm{v}}\frac{\pi}{3}\left\{\frac{3D^2}{4} + \frac{1}{4}\left(\frac{D^3 - 2DD_{\mathrm{p}}^2}{\sqrt{D^2 - D_{\mathrm{p}}^2}}\right) - \frac{D_{\mathrm{p}}^2 D}{8\sqrt{D_{\mathrm{d}}^2 - D_{\mathrm{p}}^2}}\right\} \tag{11}$$

(f) *Liquid inertia force (F_{li}):* As the bubble grows, the surrounding liquid resists movement. Hence, a force is imparted on the bubble resisting its growth. The liquid inertia can be expressed as

$$F_{\mathrm{li}} = V_{\mathrm{b}}\rho_{\mathrm{l}}\frac{\mathrm{d}v_{\mathrm{n}}}{\mathrm{d}t} \tag{12}$$

For inertia driven growth, the velocity of the bubble front is constant (zero acceleration). Hence there is no inertia force.

At departure, the instantaneous diameter of the bubble $D = D_{\mathrm{d}}$ and hence solving a force balance equation will give the bubble departure diameter. The buoyancy force and the lift force tend to pull the bubble off the pore, where as the other three forces (growth, surface tension and bubble inertia) keep it attached. Hence the bubble departs when

$$F_{\mathrm{duy}} + F_{\mathrm{st}} + F_{\mathrm{bi}} = F_{\mathrm{B}} + F_{\mathrm{L}}.$$

2.2. Modeling tunnel heat transfer

The tunnel heat transfer is modeled similar to Chien and Webb [4] with few modifications. The meniscus along one corner is shown in Fig. 4a and the local thickness is calculated perpendicular to the liquid–vapor interface. A one-dimensional heat conduction analysis gives

$$q''_{\mathrm{t}} = \frac{k_{\mathrm{l}}}{\delta(\phi)}(T_{\mathrm{w}} - T_{\mathrm{s}}) \tag{13}$$

where T_{s} is the local saturation temperature of the liquid and may not be same as the bulk saturation temperature. When the liquid film becomes very thin, the satu-

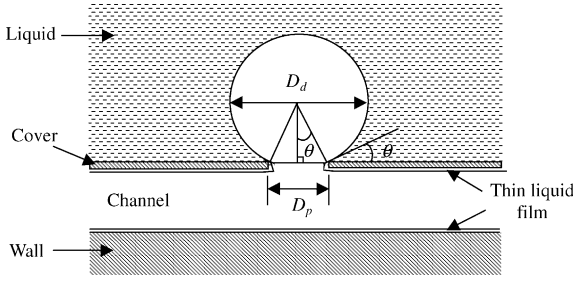

Fig. 3. Growing bubble on a surface pore [4].

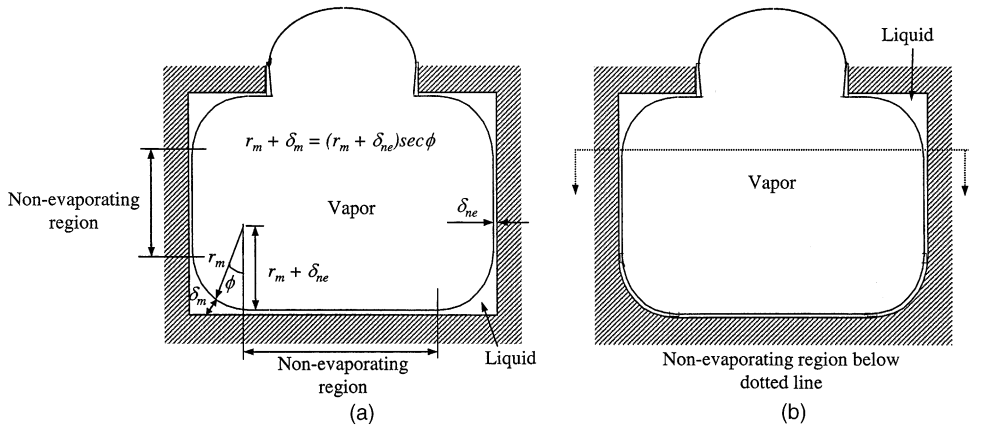

Fig. 4. Liquid meniscus along the corners of the tunnel (a) sharp corners ($N_m = 4$), (b) rounded corners ($N_m = 2$).

ration temperature elevates due to capillary pressure and disjoining pressure [13]. Based on this assumption, the local saturation temperature can be expressed as [4]

$$T_s = T_{sat}\left(1 + \frac{\sigma/r_m + C_H/\delta^3}{h_{fg}\rho_l}\right) \tag{14}$$

where C_H is the Hamaker constant. Dasgupta et al. [13] carried out experiments to determine the equilibrium disjoining pressure from thin evaporating menisci and found that the Hamaker constant is a function of the liquid surface combination and the wall superheat value. For an octane/silicon system they found the Hamaker constant to be in the range $3.0 - 0.69 \times 10^{-21}$ J, for wall superheats in the range 0.000045–0.002 °C. Since no information was avilable in literature for FC-72 and similar low surface tension fluids, a constant of 1×10^{-13} was used in the current model. The predictions for frequency and nucleation site density were found to be fairly sensitive to the value of Hamaker constant. A value of 1×10^{-13} resulted in the best predictions for heat flux, nucleation site density and frequency. Chien and Webb [4] used a value of 2×10^{-12} for their model and the reasoning seems to be similar to that presented above, although not explicitly stated. More fundamental studies are required to accurately evaluate this constant for low surface tension fluids.

The tunnel heat transfer rate can be evaluated as

$$\frac{dQ_t}{dt} = \int_0^{A_m} \frac{k_l(T_w - T_s)}{\delta(t,\phi)}\, dA \tag{15}$$

where A_m is the meniscus area per unit length. Chien and Webb [4] did not include the local wall superheat term inside the integral. For fairly low wall superheat values, the variation in the local saturation temperature was found to have minimal effect on the heat transfer predictions. This justifies their assumption of a uniform local wall superheat equivalent to the bulk wall superheat. However, in the current study, the wall superheat values are as high as 12 °C and hence this term was evaluated as a function of the local meniscus thickness.

From Fig. 4a, for a small time step Δt, if the radius of the meniscus is assumed to be constant, the local meniscus thickness can be calculated using the following expression:

$$\delta(t,\phi) = [r_m(t) + \delta_{ne}]\sec(\phi) - r_m(t) \tag{16}$$

where δ_{ne} is the film thickness at which no more evaporation takes place. The non-evaporation thickness is expressed as

$$\delta_{ne} = \left(\frac{C_H T_{sat}}{\rho_l h_{fg} \Delta T_{sup}}\right)^{1/3} \tag{17}$$

For a small increment in the angle ($d\phi$), the area dA can be expressed as

$$dA = LN_m r_m d\phi \tag{18}$$

The latent heat transfer in the tunnel is given as

$$Q_t = 2LN_m \int_0^{1/f}\int_0^{\pi/4} \frac{k_l(T_w - T_s)}{[r_m(t) + \delta_{ne}]\sec(\phi) - r_m(t)} \times r_m(t)\, d\phi\, dt \tag{19}$$

The above equation requires the initial meniscus radius ($r_{m,i}$) to begin the calculation. The procedure for calculating the initial meniscus radius is similar to one developed by Chien and Webb [4] and is presented in a later section. Once the initial meniscus radius is evaluated, using small increments in time and angle ($d\phi$), Eq. (19) is evaluated by numerical integration. The meniscus radius is updated at every time step by a new value calculated using the following equation:

$$r_{m,new} = \left[r_{m,old}^2 - \frac{\Delta V_l}{LN_m(1 - \pi/4)}\right]^{1/2} \tag{20}$$

where ΔV_l is the volume of liquid evaporated in the small time increment. Using Eqs. (15)–(19), this can be expressed as

$$\Delta V_l = \Delta t \frac{2LN_m}{h_{fg}\rho_l} \times \int_0^{\pi/4} \frac{k_l(T_w - T_s)}{[r_m(t) + \delta_{ne}]\sec(\phi) - r_m(t)} r_m(t)\,d\phi \quad (21)$$

2.3. Modeling the waiting period

The following assumptions are made for modeling the waiting period:

(a) At the initiation of the waiting period, the vapor in the tunnel is in saturated state corresponding to the system pressure.
(b) The vapor behaves as an ideal gas.
(c) The density and volume of vapor inside the tunnel vary linearly with time.

Based on the first assumption, the initial conditions are $P_{v0} = P_{sat}$, $T_{v0} = T_{sat}$, and $\rho_{v0} = \rho_v$. At the end of waiting period, the pressure inside the tunnels is equal to the breakthrough pressure at the pore and is given by

$$P_{v1} = P_{v0} + \frac{4\sigma}{D_p} \quad (22)$$

The Clausius–Clayperon equation is expressed as

$$\frac{dT_v}{dP_v} = \frac{T_{v0}}{\rho_{v0}h_{fg}} \quad (23)$$

and the equation of state for an ideal gas is

$$P_v = \rho_v \mathbf{R} T_v \quad (24)$$

Combining Eqs. (22)–(24), the temperature and density at the end of waiting period can be evaluated as

$$T_{v1} = T_{v0} + \left(\frac{4\sigma}{D_p}\right)\frac{T_{v0}}{\rho_{v0}h_{fg}} \quad (25)$$

$$\rho_{v1} = \frac{\rho_{v0}\mathbf{R}T_{v0} + 4\sigma/D_p}{\mathbf{R}\left(T_{v0} + \frac{4\sigma}{D_p}\frac{T_{v0}}{\rho_{v0}h_{fg}}\right)} \quad (26)$$

A heat balance equation can be written for heat transfer in the tunnel as

$$\frac{dQ_t}{dt} = h_{fg}\frac{dm_v}{dt} \quad (27)$$

where dm_v/dt is the rate of vapor mass added in the tunnel. This can be expressed as

$$\frac{dm_v}{dt} = V_{vm}\frac{d\rho_v}{dt} + \rho_{vm}\frac{dV_v}{dt} \quad (28)$$

Nakayama et al. [3] introduced an empirical constant to account for the change in meniscus radius and modeled the left-hand side of Eq. (27) as

$$\frac{dQ_t}{dt} = k_l C_{tl}(T_{wall} - T_v) \quad (29)$$

Chien and Webb [4] modified this by using Eq. (15) and hence the empirical constant C_{tl} was eliminated. However, both the authors modeled the change in vapor mass similarly and Eq. (27) was expressed as

$$\int_0^{\Delta t_w} \frac{dQ_t}{dt}\,dt = \Delta T_{sup} V_{vm} h_{fg}\left\{\frac{\rho_{vm}(h_{fg} - \mathbf{R}T_{v0})}{\mathbf{R}T_{v0}^2} \times \ln\left(\frac{T_v - T_{v0}}{T_{wall} - T_{v1}}\right) + \frac{\rho_{vm}}{\Delta T_{t1}}\ln\left(\frac{V_{v1}}{V_t}\right)\right\} \quad (30)$$

The current study follows a simpler approach by assuming that the density and volume vary linearly with time. Hence for the waiting period (Δt_w), the following expressions hold:

$$\frac{d\rho_v}{dt} = \frac{(\rho_{v1} - \rho_{v0})}{\Delta t_w} \quad (31)$$

$$\frac{dV_v}{dt} = \frac{(V_{v1} - V_{v0})}{\Delta t_w} \quad (32)$$

Combining Eqs. (27), (28), (31) and (32), the final expression for latent heat transfer rate inside the tunnels is

$$\frac{dQ_t}{dt} = h_{fg}\left\{V_{vm}\frac{(\rho_{v1} - \rho_{v0})}{\Delta t_w} + \rho_{vm}\frac{(V_{v1} - V_{v0})}{\Delta t_w}\right\} \quad (33)$$

The difference in the right-hand side terms in Eqs. (30) and (33) was less than 1% for all the structures used in this study. Integrating Eq. (33) from $t = 0$ to Δt_w, one obtains

$$\int_0^{\Delta t_w} \frac{dQ_t}{dt}\,dt = h_{fg}\{V_{vm}(\rho_{v1} - \rho_{v0}) + \rho_{vm}(V_{v1} - V_{v0})\} \quad (34)$$

The right-hand side of Eq. (34) depends only on the geometry of the structure. The left-hand side of Eq. (34) is evaluated similar to Eq. (19) and solving the equation provides the waiting period. The variables on the right-hand side of Eq. (34) are expressed as $V_{v0} = V_t$ and $V_{v1} = V_{v0} + N_p(D_p^2 t_c/4 + D_p^3/12)$, where V_t is the tunnel volume, and t_c is the thickness of the cover plate. For the structures used by Nakayama et al. [3] and Chien and Webb [4], the thickness of the cover plate was much lesser than the pore size and hence this term was neglected. In the current structures, the distance between the pore and the top surface is approximately equal to the height of the channels (see Fig. 5) and hence this term has to be included ($t_c = H_t$). The terms V_{vm} and ρ_{vm} can be expressed as $V_{vm} = (V_{v0} + V_{v1})/2$ and $\rho_{vm} = (\rho_{v1} + \rho_{v0})/2$.

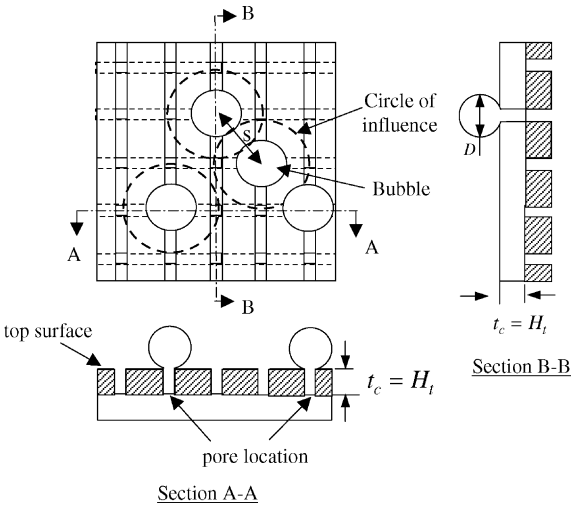

Fig. 5. Bubbles growing on the enhanced structures used in the current study (s = average separation distance).

2.4. Modeling the growth period

As mentioned earlier, the boiling from plain surfaces is typically modeled as heat transfer controlled and the instantaneous bubble radius $R \sim t^{1/2}$. As discussed by Chien and Webb [9], the growth of bubble from structured surfaces is very different from boiling on plain surfaces and is typically inertia controlled. They modified the growth equation of Mikic et al. [14] to evaluate the growth rate as

$$\frac{dR}{dt} = C_{tg}\sqrt{\left(\frac{\pi}{7}\frac{h_{fg}\rho_v \Delta T_{sup}}{\rho_l T_{sat}}\right)\left(\frac{D_d - D_p}{D_d + D_p}\right)} \tag{35}$$

The constant C_{tg} was evaluated as 0.0296 based on a curve fit of the bubble growth data. Visualization results for the current structure [11] also show that the instantaneous bubble diameter varied linearly with time. The above correlation was used for the current model and good agreement with the experimental data was achieved (for details see [15]). The bubble diameter at the beginning of the growth period is equal to the pore diameter and at time $t = \Delta t_g$, it is equal to D_d. Integrating Eq. (35) within these limits gives

$$\Delta t_g = \frac{1}{C_{tg}}\sqrt{\left(\frac{7}{\pi}\frac{\rho_l T_{sat}}{h_{fg}\rho_v \Delta T_{sup}}\right)\left(\frac{D_d + D_p}{D_d - D_p}\right)\left(\frac{D_d - D_p}{2}\right)} \tag{36}$$

Differentiating Eq. (2) with respect to 't' and comparing with Eq. (35) gives the expression for the constant A'. As the bubble departure diameter is not known a priori, the process becomes iterative.

2.5. Modeling nucleation site density

The vapor generated as a result of evaporation in the tunnels is ejected out in the form of bubbles from the pores. From a mass balance the number of bubbles formed on the surface can be expressed as

$$N_b = \frac{Q_t}{\rho_v h_{fg} f(\pi D_d^3/6)} \tag{37}$$

Dividing by the external area will give the nucleation site density

$$n_s = \frac{Q_t}{\rho_v h_{fg} f(\pi D_d^3/6) A_{ex}} \tag{38}$$

2.6. Modeling external heat transfer

Several authors have investigated the enhanced convection effect as a result of the intermittent bubble formation on plain surfaces. Mikic and Rohsenow [16] developed a model based on the intermittent nature of the boiling process. According to the model, a bubble departing from the heated surface removes a part of the superheated layer within an area of influence equal to twice the bubble departure diameter. Quenching of the exposed area with fluid at the bulk temperature immediately follows this. Hence, the problem was assumed to be similar to one-dimensional transient conduction through a semi-infinite solid. The time averaged heat flux was evaluated as

$$q''_{ex} = 2\sqrt{\pi k_l \rho_l c_p f} D_d^2 n_s \Delta T_{sup} \tag{39}$$

Tien [17] modeled the external convection based on a hydrodynamic similarity between the flow field associated with a rising bubble column and an inverted stagnation flow. Based on experimental data from other authors, the external convective heat flux was expressed as

$$q''_{ex} = 61.3 k_l n_s^{1/2} Pr^{1/3} \Delta T_{sup} \tag{40}$$

Haider and Webb [5] evaluated the above two models with visualization data of Chien and Webb [9] and found that both models under predict the data by as much as 70%. Haider and Webb [5] developed a model, which takes into account a steady state convection term in addition to the transient conduction term and expressed the external heat flux as

$$q''_{ex} = 2\sqrt{\pi k_l \rho_l c_p f} D_d^2 n_s \Delta T_{sup}\left\{1 + \left(\frac{0.66\pi c}{Pr^{1/6}}\right)^n\right\}^{1/n} \tag{41}$$

Based on data of Chien and Webb [9], a value of 6.42 was recommended for the constant 'c' and 2 for the constant 'n'. Eq. (41) was used to predict the external heat flux for the structures used in the authors' visualization study [11]. The model resulted in significant

overprediction (as high as 500%). The use of a universal constant of 6.42 for all heat fluxes does not seem to be an appropriate one in Eq. (41). The current study proposes a variable value for 'c' which is a function of the wall superheat. Based on the visualization data, a third order polynomial was evaluated such that the difference in the predicted and experimental heat flux values were within acceptable limits. The proposed function for 'c' is

$$c = a_0 + a_1(\Delta T_{\text{sup}}) + a_2(\Delta T_{\text{sup}}^2) + a_3(\Delta T_{\text{sup}})^3 \tag{42}$$

the constants are $a_0 = 6.58$, $a_1 = -1.1612/^\circ\text{C}$, $a_2 = 0.0782/^\circ\text{C}^2$ and $a_3 = -0.0018/^\circ\text{C}^3$.

Eq. (42) was used to predict the external heat flux for the data listed in Haider and Webb [5] and the current flow visualization data. The error in the predictions is within ±40% for almost all the data points (for details see [15]).

As the number of bubbles grows on the heated surface, the average distance between two adjacent bubbles reduces. For a distance greater than two times the bubble departure diameter the assumption of an influence area twice the diameter of a bubble is valid. However, if the average separation distance falls below twice the bubble departure diameter, the influence areas will overlap. Judd and Lavdas [18] showed that as the vapor coverage increases on the surface, the influence area reduces. Based on a curve fit to the experimental data of Judd and Hwang [19], they proposed an influence factor as a function of the fractional boiling area. In the current study, all the structures have pores on a uniform grid. For a given nucleation site density, the average separation distance between two adjacent bubbles can be evaluated as

$$s = \frac{1}{\sqrt{n_s}} \tag{43}$$

It is assumed that there is almost no phase lag between the bubbles departing from adjacent pores. Hence, as the distance 's' falls below twice the bubble departure diameter, the area of influence reduces and will be no more than a circle of diameter equal to the separation distance itself. This has been included in the external heat flux model used in the current study.

2.7. Prediction procedure

Based on the equations outlined, a prediction procedure was developed. The steps in predicting the essential parameters are as follows:

(1) Calculate the bubble departure diameter (D_d) using Eqs. (3), (4), (7), (9), (11) and (35).
(2) Calculate the initial meniscus radius $r_{m,i}$ from the correlation developed (procedure and equation in next section).
(3) Calculate the latent heat transfer inside the tunnel during the waiting period ($Q_{t,w}$) and also calculate the waiting period (Δt_w). Small time steps were chosen to solve Eq. (34) until the right-hand side and left-hand side values matched within 5%. After every time step, a new meniscus radius ($r_{m,new}$) was calculated using Eqs. (20) and (21). The meniscus radius at the end of the waiting period ($r_{m,g}$) becomes the initial value for the growth period.
(4) Calculate the growth period (Δt_g) using Eq. (36).
(5) Calculate the latent heat transfer inside the tunnel during the growth period ($Q_{t,g}$) by dividing the entire growth period into small time increments and stepping through them similar to step 3.
(6) Calculate the frequency of bubble departure (f) as $1/(\Delta t_w + \Delta t_g)$.
(7) Calculate the total tunnel heat flux (q''_t) as $(Q_{t,w} + Q_{t,g})f/A_{ex}$.
(8) Calculate the nucleation site density (n_s) using Eq. (38).
(9) Calculate the external connective heat flux (q''_{ex}) using Eqs. (41) and (42).
(10) The total heat flux is calculated as $q'' = q''_t + q''_{ex}$.

2.8. Correlating the initial meniscus radius ($r_{m,i}$)

The results from the visualization experiments were used to develop an expression for calculating the initial meniscus radius. An initial guess for $r_{m,i}$ was chosen and the procedure outlined above followed to calculate the total heat flux. The predicted heat flux was compared to the experimental value at the same wall superheat. The procedure was repeated till $q''_{pred} \sim q''_{exp}$. The total change in volume of liquid per unit length (ΔA_{cyc}) was then calculated using the following equation (per bubble cycle):

$$\Delta A_{cyc} = (r_{m,i}^2 - r_{m,e}^2)N_m\left(1 - \frac{\pi}{4}\right) \tag{44}$$

The final meniscus radius ($r_{m,e}$) was assumed to attain a value where no further evaporation takes place [4]. This is also referred to as the non-evaporating meniscus radius (r_{ne}). The non-evaporating meniscus radius is dependent only the fluid properties and the wall superheat and is expressed as

$$r_{ne} = \frac{\sigma}{\Delta T_{sup}}\left(\frac{dT_v}{dP_v}\right) \tag{45}$$

The term dT_v/dP_v is evaluated using Eq. (23). The next step was to correlate the calculated data for ΔA_{cyc} based on the geometric parameters. The liquid volume change per unit length depends on the geometric parameters, wall superheat and the fluid properties. Since only FC-72 was used in the above study, the correlation developed here is only valid for this fluid. The geometric

factors that influence the amount of liquid inside the tunnels are the pore diameter, pore pitch, tunnel height and tunnel width. Since the tunnel width in the current structures is the same as the pore size, only one of the factors is sufficient to capture either variable. The number of menisci (N_m) depends on the cross-section of the tunnel. For tunnels with sharp corners at the base (Fig. 4a), $N_m = 4$ (two on top and two at the bottom) and for tunnels with a curved base (Fig. 4b), $N_m = 2$ (at the top only). In this study, the structures fabricated using wet-etching had a rectangular base. Structures fabricated using wafer dicing had a rounded base. Hence this is an added parameter that was included in the correlation. The final form of the correlation was assumed to be as follows:

$$\Delta A_{cyc} = C_a(\Delta T_{sup})^{a1}(D_p^2)^{a2}P_p^{a3}H_t^{a4}N_m^{a5} \quad (46)$$

The data points from visualization studies were used to develop several different correlations. The one that was used for carrying out the predictions had the following constants:

$$C_a = 2.4322 \times 10^{-6}, \quad a1 = 1.266, \quad a2 = 0.428,$$
$$a3 = -0.138, \quad a4 = 0.525, \quad a5 = 0.026$$

The liquid intake depends on the total area of pores on the structure. Clearly, as the number of pores increases, there will be more liquid supply into the tunnel. The negative sign of the exponent ($a3$) for the fin pitch (P_p) reflects this. Similarly, for a constant pitch, a larger pore size will result in better supply of liquid. This is indicated by the positive exponent ($a2$) for the pore diameter (D_p).

The model was developed primarily for the isolated bubble regime. The assumption was that the individual bubbles departing the surface do not coalesce either laterally or vertically. If either phenomenon occurs, the prediction of the bubble departure diameter is no more valid. Also a coalesced bubble may hover around for a longer time or get pulled out by a departing bubble from an adjacent site. Hence the point of coalescence (either vertical or lateral) is a physically meaningful criterion to define the upper limit of this model. The criterion for lateral coalescence is provided by Eq. (43). When the average separation distance is equal to the bubble departure diameter, lateral coalescence will occur. The vertical coalescence was defined using an approach outlined by Zuber [20]. The study shows that the condition for vertical coalescence can be expressed in terms of a dimensionless group 'B' as

$$B = \frac{\pi}{6}\frac{n_s D_d^3 f}{v_t} = \frac{1}{4} \quad (47)$$

where v_t is the terminal velocity of a bubble in a liquid pool. The terminal velocity is expressed as

$$v_t = 1.53\left[\frac{\sigma g(\rho_l - \rho_v)}{\rho_l^2}\right]^{1/4} \quad (48)$$

This criterion was included in the model described above and the predictions stopped when either of the two limits was reached.

3. Results of semi-analytical model

The semi-analytical model described in the previous section was used to predict the bubble departure, frequency, nucleation site density and the total heat flux dissipated from the enhanced structures. The predicted values were compared to the experimental data and salient results are included below.

3.1. Prediction of bubble departure diameter

A comparison of the predicted and experimental values for bubble departure diameter is shown in Fig. 6. The nomenclature of the structures are to be interpreted as follows: the first letter 'S' denotes structures made in silicon, the number following that gives the pore diameter (in millimeters). The number following the pore diameter is the pore pitch (in millimeters) and finally the last letter denotes the method of fabrication ('D'—wafer dicing and 'W'—wet etching). The results in Fig. 6 show very good agreement between the predicted and experimental values. The absolute error in predicting the departure diameter was within a range of +10% to −6%. Another useful statistic referred to as the relative deviation is defined as [7]

$$\text{r.d.} = \frac{\sum_{k=1}^{N}\frac{|D_{d,pred,k} - D_{d,exp,k}|}{D_{d,exp,k}}}{N} \times 100 \quad (49)$$

where N is the number of data points. The relative deviation for the current model was 2.4% (based on 24

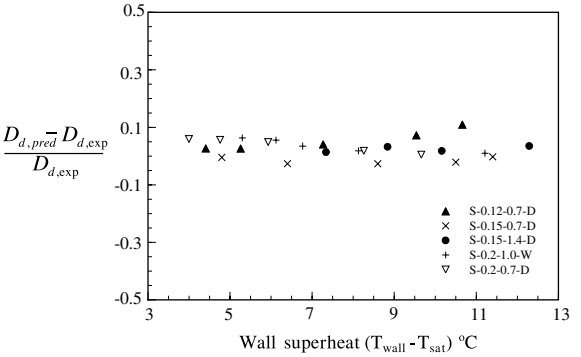

Fig. 6. Comparison of bubble departure diameter—prediction vs. experiments.

flow visualization data points) showing the effectiveness of the current model. The individual force data showed that at low wall superheat values (2–6 °C), the growth force, buoyancy force, surface tension force and lift force are of equal magnitude. However, at intermediate wall superheat values (8–12 °C), the dynamic forces (growth force and lift force) become the dominant ones. Clearly, neglecting these forces in a bubble departure model will lead to erroneous results.

3.2. Prediction of frequency

A comparison of the predicted values for frequency and experimentally observed values is shown in Fig. 7. The curves show that at low wall superheats (4–6 °C) the absolute error is within ±30%. However, at intermediate wall superheats (8–12 °C), the model overpredicts by as much as 60% (for at least two data points). The relative deviation for the set of 24 data points using the current model was 24%. The predicted values show that the frequency increases monotonically with an increase in the wall superheat values. However, the experiments show a reduction in the frequency, at intermediate wall superheat values (8–12 °C).

The total cycle time for a bubble to form and depart is made up of the waiting time and the growth time. Under prediction of either of these quantities will lead to an overprediction in the frequency. A comparison of the predicted and experimentally measured values of the growth period shows that the absolute error is within +20% at all wall superheat values. Hence, an underprediction in the waiting period was the main reason for the overprediction in frequency for the two data points (mentioned above). The evaporation inside the tunnels was found to be sensitive to the Hamaker constant. This affects the prediction in the waiting period directly. A better understanding of the Hamaker constant is required and an improvement in this factor will improve the frequency predictions.

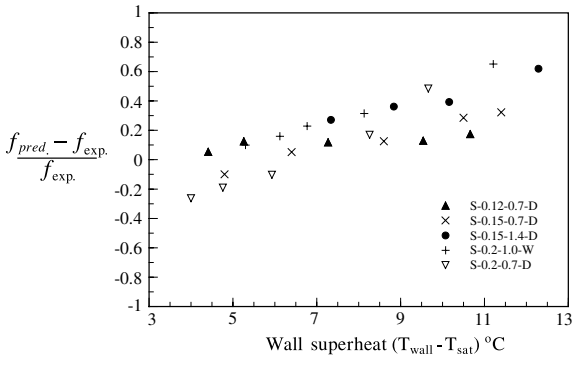

Fig. 7. Comparison of frequency—prediction vs. experiments.

3.3. Prediction of nucleation site density

A comparison of the predicted values for nucleation site density with that observed experimentally is shown in Fig. 8. The absolute error in the prediction lies within a range of ±40%. The relative deviation in the nucleation site density for the current set of data points was 20%. The bubbles form on the external surface as a result of the evaporation in the tunnels. Hence any uncertainty in the prediction of evaporation inside the tunnels translated in an uncertainty in the prediction of the nucleation site density.

3.4. Prediction of heat flux

A comparison of the predicted values to experimental ones, for structures with a pore size of 150 μm is shown in Fig. 9. The data show that the prediction for structure 'S-0.15-1.4-D' was fairly accurate. The maximum error in prediction for this structure was +14% at the lowest wall superheat (7.3 °C). This error reduced at higher wall superheat (17.3 °C) to approximately −1%. The maximum error in the predictions for 'S-0.15-0.7-D' was +33% at the lowest wall superheat (4.5 °C). The error reduced monotonically to almost −4% at a wall superheat of 12.5 °C. A similar trend was observed for structure 'S-0.15-0.5-W'. The maximum error in this case was 50% at a wall superheat of 4.4 °C and the error reduced monotonically to −4.9% at a wall superheat of 10.9 °C. The total heat flux is a sum of the tunnel heat flux and the external heat flux. The tunnel heat flux depends on the initial meniscus radius and the rate of evaporation. The external heat flux depends on the nucleation site density, bubble departure diameter and the influence factor (when the average separation distance falls below twice the departure diameter). And frequency affects both the components of heat flux. The predictive error associated with the bubble departure diameter, frequency and nucleation site density has already been discussed in the previous sections. A combination of any

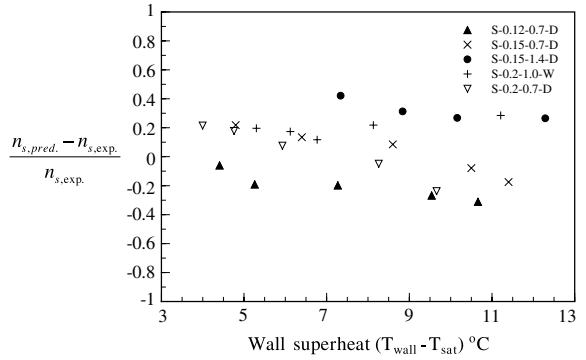

Fig. 8. Comparison of nucleation site density—prediction vs. experiments.

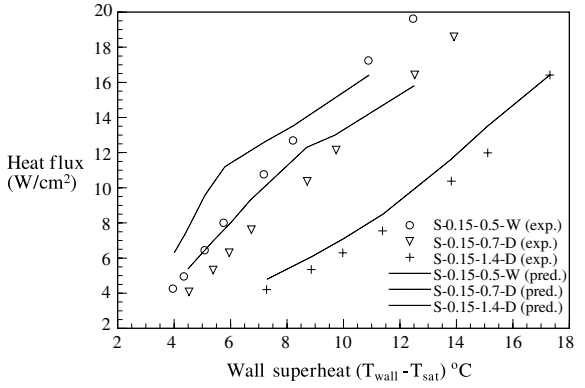

Fig. 9. Comparison of predicted and experimental heat flux for all structures with $D_p = 150$ μm.

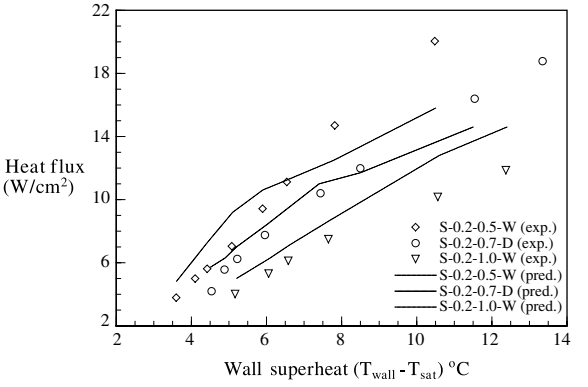

Fig. 10. Comparison of predicted and experimental heat flux for all structures with $D_p = 200$ μm.

of these factors could have resulted in the errors for heat flux prediction. The model's strength lies in the prediction of the trend observed in the experiments. The predictions do show that increasing the number of pores results in higher heat dissipation (at the same wall superheat values).

The predicted results (Fig. 9) show a distinct change in slope for 'S-0.15-0.5-W' and 'S-0.15-0.7-D'. This change in slope coincides with the point where the average separation distance falls below twice the bubble departure diameter. One of the assumptions of the external heat flux model was that the bubbles departing from adjacent sites did not have a phase lag. Hence the area of influence was assumed to be no more than a circle of diameter equal to the separation distance itself. In reality, there will be some phase difference between the bubbles and hence the influence diameter will be more than the average separation distance. This will make the transition in the predicted curves smoother and reduce the underprediction at the higher wall superheat values. However, this requires some validation and quantification through more fundamental flow visualization studies. An alternative approach was to curve fit the external heat flux to arrive at an empirical influence factor similar to Judd and Lavdas [18]. However, this would have introduced another empirical constant (or function). To reduce the empiricism in the model, the former approach was chosen.

Comparison of the predicted values to experimental ones, for structures with a pore size of 200 μm is shown in Fig. 10. Once again the trends were similar to that observed with 150 μm structures. The predictive error was in the range ±30%. Similar predictions were carried out for other structures (for details see [15]).

3.5. Optimization of enhanced structure

The ultimate goal of the model is to carry out optimization of the enhanced structure geometry. The current model was used to study the effect of changing the geometrical parameters (pore diameter and pore pitch) to maximize heat transfer. In the accompanying paper, it is shown that increasing the pore diameter or the pore density increases the heat transfer, for the same wall superheat. For enhanced structures of similar overall size, as the pore diameter is increased, the number of pores per channel and hence the pore density decreases (assuming that the wall thickness between adjacent channels is the same). These have competing effects on the heat transfer and hence an optimum could be found where heat transfer is maximum. Tables 1–3 show the heat flux from structures with three different wall thicknesses (0.1–0.7 mm). As mentioned earlier the current model was developed for suction–evaporation mode. For cases where the liquid floods the channels, the results in the table mention that. The table also mentions if a coalescence criterion was reached. The results show that for a wall thickness of 0.3 mm, the optimum pore diameter is approximately 100 μm. However for wall thickness of 0.7 mm, the optimum is approximately 200 μm. Comparing all the structures simultaneously reveals that a smaller pore diameter with lots of pores results in maximum heat transfer, but this also makes the structure structurally weak. In addition impurities in the fluid will eventually clog the very fine pores. Hence while designing an optimum structure factors other than heat transfer will also have to be considered.

4. Conclusions

A semi-analytical model that predicts the departure diameter, frequency, nucleation site density and total heat flux for isolated bubble regime has been developed. The model assumes that the boiling mode is 'suction–evaporation' and the meniscus evaporation within the

Table 1
Predicted heat dissipation for enhanced structures with wall thickness = 0.1 mm

ΔT_{sup}	Heat flux (W/cm^2)			
	$D_p = 50$ μm, $P_p = 0.15$ mm	$D_p = 100$ μm, $P_p = 0.2$ mm	$D_p = 200$ μm, $P_p = 0.3$ mm	$D_p = 300$ μm, $P_p = 0.4$ mm
2.5	5.6	4.8	Flooded	Flooded
3.75	10.2	7.9	5.6	3.8
5	12.7	10.3	8.8	6.2
7.5	15.8	13.7	10.8	9
10	Coalescence	Coalescence	13.9	11.8

Table 2
Predicted heat dissipation for enhanced structures with wall thickness = 0.3 mm

ΔT_{sup}	Heat flux (W/cm^2)			
	$D_p = 50$ μm, $P_p = 0.15$ mm	$D_p = 100$ μm, $P_p = 0.2$ mm	$D_p = 200$ μm, $P_p = 0.3$ mm	$D_p = 300$ μm, $P_p = 0.4$ mm
2.5	2.1	2.2	2	Flooded
3.75	4.4	4.6	4.3	3.6
5	6.8	7.1	6.6	5.7
7.5	11.1	11.8	10	8.6
10	13.9	13.6	12	10.6
12.5	15.7	16.1	14.8	13.2

Table 3
Predicted heat dissipation for enhanced structures with wall thickness = 0.7 mm

ΔT_{sup}	Heat flux (W/cm^2)			
	$D_p = 50$ μm, $P_p = 0.15$ mm	$D_p = 100$ μm, $P_p = 0.2$ mm	$D_p = 200$ μm, $P_p = 0.3$ mm	$D_p = 300$ μm, $P_p = 0.4$ mm
2.5	0.9	1	1	1
3.75	1.9	2	2.1	2.1
5	2.9	3.1	3.3	3.3
7.5	4.8	5.3	5.6	5.6
10	6.5	7.6	8.1	7.9
12.5	8.6	10.4	11.4	11.2
15	10.9	14	15.3	14.5
20	13.2	16.8	17.7	17.4

tunnel results in all the vapor formation. The salient improvements over existing models and conclusions based on the predictions are

(a) The dynamic forces have been included in the prediction of the bubble departure diameter and the magnitude of individual forces shows that these dominate at higher wall superheats.
(b) Local variation of the liquid saturation temperature due to variation in the meniscus thickness has been included in the tunnel heat transfer component. The Hamaker constant affects the evaporation rate (Eqs. (15)–(17)) inside the tunnels and hence all the other components that depend on the tunnel heat transfer. The sensitivity of predictions to this constant has been pointed out.
(c) A wall superheat dependent constant 'c' for the convective component of external heat flux has been proposed. A physically meaningful criterion for bubble coalescence has been proposed and defines the upper limit of the model.
(d) The current model predicts the bubble departure diameter fairly accurately. It captures the increase in bubble diameter at higher wall superheats.
(e) The frequency prediction is within ±30% at low wall superheat values. However, underprediction in the waiting time results in errors of as much as 60% for a couple of data points. The prediction for nucleation site density was found to be within ±40%. The sensitivity of the prediction to the value of Hamaker constant is outlined.
(f) The heat flux was predicted within ±50%. The important aspect of the model is that it captures the trends fairly well. The predictions show a rise in the heat dissipation with an increase in the number of pores (reduction in the pore pitch). The model also predicts higher heat dissipation for a larger pore diameter.

Acknowledgements

This work was performed while the authors were at the University of Maryland, College Park. The authors would like to acknowledge support of this work through the members of CALCE Electronic Products and Systems Center and the Defense Advanced Research Projects Agency under the HERETIC program.

References

[1] J.R. Thome, Enhanced Boiling Heat Transfer, Hemisphere Publishing, New York, 1990.
[2] R.L. Webb, Principles of Enhanced Heat Transfer, John Wiley & Sons, New York, 1994.
[3] W. Nakayama, T. Daikoku, H. Kuwahara, T. Nakajima, Dynamic model of enhanced boiling heat transfer on porous surfaces. Part II. Analytical modeling, ASME J. Heat Transfer 102 (1980) 451–456.
[4] L.-H. Chien, R.L. Webb, A nucleate boiling model for structured enhanced surfaces, Int. J. Heat Mass Transfer 41 (14) (1998) 2183–2195.
[5] I. Haider, R.L. Webb, A transient micro-convection model of nucleate pool boiling, Int. J. Heat Mass Transfer 40 (15) (1997) 3675–3688.
[6] J.F. Klausner, R. Mei, D.M. Bernhard, L.Z. Zeng, Vapor bubble departure in forced convection boiling, Int. J. Heat Mass Transfer 36 (3) (1993) 651–662.
[7] L.Z. Zeng, J.F. Klausner, R. Mei, A unified model for the prediction of bubble detachment diameters in boiling systems—I. Pool boiling, Int. J. Heat Mass Transfer 36 (9) (1993) 2261–2270.
[8] P.R. Sharma, Determination of heat transfer rates in nucleate pool boiling of pure liquids for a wide range of pressure and heat flux, in: Proceedings of the 11th International Heat Transfer Conference, Kyongju, South Korea, vol. 2, 1998, pp. 467–472.
[9] L.-H Chien, R.L. Webb, Measurement of bubble dynamics on an enhanced boiling surface, Exp. Thermal Fluid Sci. 16 (3) (1998) 177–186.
[10] N.I. Kolev, The influence of mutual bubble interaction on the bubble departure diameter, Exp. Thermal Fluid Sci. 8 (1994) 167–174.
[11] C. Ramaswamy, Y. Joshi, W. Nakayama, W.B. Johnson, High speed visualization of boiling from an enhanced structure, Int. J. Heat Mass Transfer 45 (2002) 4761–4771.
[12] A.P. Hatton, D.D. James, T.L. Liew, Measurement of bubble characteristics for pool boiling from single cylindrical cavities, in: U. Grigull, E. Hahne (Eds.), Heat Transfer, vol. 5, 1970, paper no. B 1.2.
[13] S. Dasgupta, J.A. Schonberg, P.C. Wayner, Investigation of an evaporating extended menisci based on the augmented Young–Laplace equation, ASME J. Heat Transfer 115 (1993) 201–208.
[14] B.B. Mikic, W.M. Rohsenow, P. Griffith, On bubble growth rates, Int. J. Heat Mass Transfer 13 (1969) 657–666.
[15] C. Ramaswamy, A compact two-phase thermosyphon employing microfabricated boiling enhancement structures, Ph.D. Dissertation, University of Maryland at College Park, MD, 1999.
[16] B.B. Mikic, W.M. Rohsenow, A new correlation of pool boiling data including the effect of heating surface characteristics, ASME J. Heat Transfer 91 (1969) 245–250.
[17] C.L. Tien, A hydrodynamic model for nucleate pool boiling, Int. J. Heat Mass Transfer 5 (1962) 533–540.
[18] R.L. Judd, C.H. Lavdas, The nature of nucleation site interaction, ASME J. Heat Transfer 102 (1980) 461–464.
[19] R.L. Judd, K.S. Hwang, A comprehensive model for nucleate pool boiling heat transfer including microlayer evaporation, ASME J. Heat Transfer 98 (1976) 623–629.
[20] N. Zuber, Nucleate boiling—the region of isolated bubbles—similarity with natural convection, Int. J. Heat Mass Transfer 6 (1963) 53–56.